Prediction of the Dual Quantum Spin Hall Insulator in the $NbIrTe_4$ Monolayer

Xiangyang Liu(柳向阳)[1,2], Junwen Lai(赖俊文)[1,2], Jie Zhan(占洁)[1,2], Tianye Yu(于天野)[2], Wujun Shi(史武军)[3,4], Peitao Liu(刘培涛)[1,2], Xing-Qiu Chen(陈星秋)[1,2*], and Yan Sun(孙岩)[1,2*]

[1]*School of Materials Science and Engineering, University of Science and Technology of China, Shenyang 110016, China*
[2]*Shenyang National Laboratory for Materials Science, Institute of Metal Research, Chinese Academy of Sciences, Shenyang 110016, China*
[3]*Center for Transformative Science, ShanghaiTech University, Shanghai 201210, China*
[4]*Shanghai High Repetition Rate XFEL and Extreme Light Facility, ShanghaiTech University, Shanghai 201210, China*

(Received 9 October 2024; accepted manuscript online 5 February 2025)

The dual quantum spin Hall insulator (QSHI) is a newly discovered topological state in the two-dimensional (2D) material $TaIrTe_4$, which exhibits both a traditional Z_2 band gap at the charge neutrality point and a Van Hove singularity (VHS) that induces a correlated Z_2 band gap with weak doping. Inspired by the recent progress in theoretical understanding and experimental measurements, a promising dual QSHI is predicted in the counterpart material of the $NbIrTe_4$ monolayer by first-principles calculations. In addition to the well-known band inversion at the charge neutrality point, two new band inversions are found after a charge density wave (CDW) phase transition when the chemical potential is near the VHS: one direct and one indirect Z_2 band gap. The VHS-induced non-trivial band gap is approximately 10 meV, significantly larger than that of $TaIrTe_4$. Furthermore, as the newly generated band gap is mainly dominated by the 4*d* orbitals of Nb, the electronic correlation effects should be stronger for $NbIrTe_4$ than for $TaIrTe_4$. Therefore, the dual QSHI state in the $NbIrTe_4$ monolayer is expected to provide a strong platform for investigating the interplay between topologies and correlation effects.

DOI: 10.1088/0256-307X/42/3/037302 CSTR: 32039.14.0256-307X.42.3.037302

1. Introduction. Two-dimensional (2D) materials with a Van Hove singularity (VHS) near the Fermi level are ideal platforms for studying the interplay between topological electronic structures and correlation effects.[1–12] As a typical layered material, the $TaIrTe_4$ monolayer was predicted to be a 2D topological insulator with a band gap of approximately 32 meV.[13–15] Very recently, a new quantum topological state of the dual quantum spin Hall insulator (QSHI) was discovered in the $TaIrTe_4$ monolayer by observing the quantized longitudinal conductance, which is rare in other QSHIs.[16] It was found that, in addition to the QSHI state at the charge neutrality point, two new non-trivial Z_2 gaps emerge when the Fermi level shifts to the VHS points owing to weak electron and hole doping effects.

Owing to the divergence of the density of states (DOSs), a charge density wave (CDW) phase transition is induced when the Fermi level shifts to the VHSs, resulting in a correlated Z_2 band gap. In contrast to the traditional Z_2 band gap, the VHS generated topological band gap is expected to be related to the novel correlated electronic topological states of the fractional quantum spin Hall effect and helical quantum spin liquid.[17–23] Although the Z_2 band gap generated by VHSs and integer-quantized longitudinal conductance exists in $TaIrTe_4$, the corresponding fractional topology and other strongly correlated topological states have not yet been observed. Therefore, it is necessary to identify additional candidate materials that host both topology and correlation.[24–33] A possible reason for the absence of strongly correlated topological phenomena in $TaIrTe_4$ is the weak electron correlation. Inspired by this, this study analyzes the dual Z_2 topological state in $NbIrTe_4$, which is an isoelectronic counterpart of $TaIrTe_4$. Due to the difference between the Ta 5*d* and Nb 4*d* orbitals near the VHSs, the electronic correlation effect is expected to be more pronounced in $NbIrTe_4$ than in $TaIrTe_4$. Thus, $NbIrTe_4$ is a good candidate material for observing correlated topological phenomena that are absent in $TaIrTe_4$. Moreover, according to previous studies on model topological materials, such as topological insulators in $(Bi/Sb)_2(Te/Se)_3$ and Weyl semimetals in (Ta/Nb)(As/P), additional material candidates are always helpful for a complete understanding of their topological states.[34–37] In addition, they are useful for the practical experimental design of new quantum topological states in realistic materials. A typical example is the design of the first experimentally observed quantum anomalous Hall effect in Cr-doped topological insulators,[38] which motivated this study to enrich the family of dual QSHIs.

2. Computational Methods. All density functional theory (DFT) calculations presented here were performed using the Vienna ab initio simulation package (VASP)[39]

*Corresponding author. Email: xingqiu.chen@imr.ac.cn; sunyan@imr.ac.cn
© 2025 Chinese Physical Society and IOP Publishing Ltd. All rights, including for text and data mining, AI training, and similar technologies, are reserved.

within the Perdew-Burke-Ernzerhof (PBE) generalized gradient approximation (GGA) for the exchange-correlation functional.[40] The projector-augmented wave method was used with a plane-wave kinetic energy cutoff of 500 eV, and the smearing width of the Gaussian smearing method was 0.05 eV. The k-point mesh had a reciprocal space resolution of $2\pi \times 0.02\text{Å}^{-1}$. The relaxation was stopped when the norms of all the forces were $< 0.01\,\text{eV/Å}$. A tight-binding Hamiltonian model was constructed using the Wannier90 package.[41] The Nb d, Te p, and Ir d orbital compositions were used to construct the real-space Hamiltonian H_r. The Hamiltonian of the CDW modulation supercell was constructed using the Fröhlich–Peierls Hamiltonian approach, $H = H_\text{r} + V\cos(Qy)\psi_\text{r}^\dagger\psi_\text{r}$.[42] Here, V represents the potential induced by the superlattice and the intra-orbital interaction was considered. The periodicity of this potential was determined by the Fermi nesting vector Q. The Fermi surface nesting function was evaluated by the imaginary part of the bare charge susceptibility under the zero-frequency limit,

$$\chi_0''(\boldsymbol{q},\omega)/\omega = \sum_{nn',\boldsymbol{k}} \delta(\varepsilon_{n,\boldsymbol{k}} - \varepsilon_0)\delta(\varepsilon_{n',\boldsymbol{k}+\boldsymbol{q}} - \varepsilon_0),$$

where δ is the Dirac-delta function. $\varepsilon_{n,\boldsymbol{k}}$ is the eigenvalue of band n at $\boldsymbol{k}$ and ε_0 is the Fermi energy. $\boldsymbol{q}$ is the nesting vector. The real part reflects the charge density stability,

$$\chi_0'(\boldsymbol{q}) = \sum_{nn',\boldsymbol{k}} \frac{f(\varepsilon_{n,\boldsymbol{k}}) - f(\varepsilon_{n',\boldsymbol{k}+\boldsymbol{q}})}{\varepsilon_{n',\boldsymbol{k}+\boldsymbol{q}} - \varepsilon_{n,\boldsymbol{k}} + i\sigma},$$

where $f(\varepsilon)$ is the Fermi–Dirac distribution, ε is the momentum-dependent energy, and σ is the broadening.[43] The edge states were calculated by iterating the surface Green's function.

3. Results and Discussion. The crystal structure of a $NbIrTe_4$ monolayer shares the same structural prototype as a 1T′-$MoTe_2$ monolayer[44] and features a sandwich-like structure, as depicted in Fig. 1(a). In this arrangement, the Nb and Ir atoms were positioned in the middle layer, forming parallel zigzag chains along the b-axis. Each Nb or Ir atom was surrounded by six Te atoms, forming a distorted octahedron. Figure 1(c) shows the energy dispersion along the high-symmetry lines [Fig. 1(b)]. A band inversion exists near the X point with a band gap of approximately 35 meV, which is in agreement with previous studies.[14,45] In addition, two VHSs were located around Γ and X, with the former above the Fermi level and the latter below the Fermi level. Correspondingly, two narrow peaks of the DOSs generated from the VHSs existed above and below the Fermi level with energies of $\sim E_\text{F} + 60$ meV and $\sim E_\text{F} - 60$ meV, respectively. For comparison, the band structure of the $TaIrTe_4$ monolayer is illustrated in Fig. 1(e), where the closed Fermi level along the Γ-X of $NbIrTe_4$ showed a flatter conduction band, as evidenced by the DOSs presented in Figs. 1(d) and 1(f). From the orbital-projected band structure and DOSs, the two VHSs below and above the Fermi level were dominated by the 4d orbitals of Nb in $NbIrTe_4$ and 5d orbitals of Ta in $TaIrTe_4$, respectively.

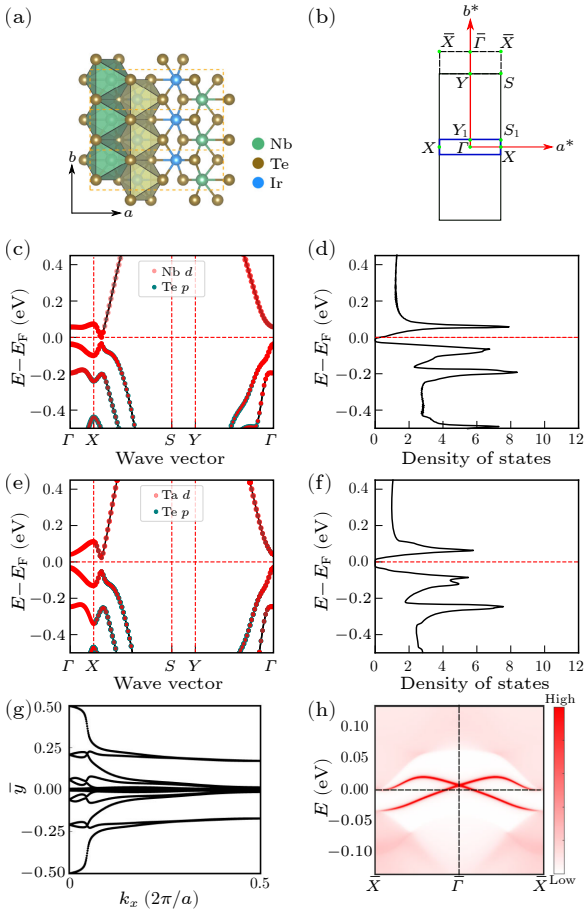

Fig. 1. Crystal and electronic structure of the $NbIrTe_4$ monolayer. (a) Top view of the crystal structure. (b) 2D Brillouin zone (BZ) and its projection along the c-axis for both the primitive cell and CDW supercell. The high-symmetry lines are denoted as follows: Γ-X-S-Y for the primitive cell, Γ-X-S_1-Y_1 for the $1 \times 20 \times 1$ supercell, and $\bar{\Gamma}$-$\bar{X}$ for the edge lines along the b-axis. (c) Energy dispersion along the high-symmetry lines of the $NbIrTe_4$ monolayer primitive cell. (d) DOSs of the $NbIrTe_4$ monolayer primitive cell. (e) Energy dispersion along the high-symmetry lines of the $TaIrTe_4$ monolayer primitive cell. (f) DOSs of the $TaIrTe_4$ monolayer primitive cell. (g) Wannier charge center evolution with the Fermi level fixed at the charge neutrality point. (h) Energy dispersion of the edge states of the $NbIrTe_4$ monolayer primitive cell.

Thus, a strong correlation was expected in the $NbIrTe_4$ monolayer. With this understanding of the electronic band structure near the Fermi level, the Bloch wavefunctions were projected into maximally localized Wannier functions (MLWFs) and effective tight-binding model Hamiltonians were constructed based on the overlaps of these Wannier orbitals.[41]

To verify the topological state, the Wannier center evolution and edge states were calculated using the chemical potential located at the charge neutrality point.[46] The evolution of the Wannier center in Fig. 1(g) had a zigzag form with a changing partner at the edges of $k_x = 0$ and π/a, which are typical features of Z_2 topological insulators.[47] Consistent with the bulk state analysis, the edge states with open boundary conditions along the b-axis showed a linear band crossing at the Γ point and connected

the occupied and unoccupied bulk bands. Hence, the Z_2 band gap at the charge neutrality point was confirmed from both the bulk band order and edge Dirac point.

To identify the detailed positions of the VHSs near the charge neutrality point, the energy dispersions of the conduction band (CB) + 2 and valence band (VB) - 2 in the entire 2D Brillouin zone (BZ) were plotted, where VB - 1 and CB + 1 refer to the indices of the highest occupied valence band and lowest conduction band, respectively, within a primitive cell, accounting for the spin. As shown in Fig. 2(a), the four VHS points on CB + 2 were located approximately at $(0.211\frac{2\pi}{a}$ and $0.024\frac{2\pi}{b})$, and their inversion and mirror partners. Similarly, the four VHS points on VB - 2 were located approximately at $(0.278\frac{2\pi}{a}$ and $0.023\frac{2\pi}{b})$, and their inversion and mirror partners.

The bare charge susceptibility was further calculated by shifting the chemical potential at $\sim E_F + 60$ and $\sim E_F - 60$ meV, which correspond to the positions of the VHSs in CB + 2 and VB - 2, respectively. Imaginary and real parts of the bare charge susceptibility at a given energy were computed and plotted as functions of $\boldsymbol{Q}$, as shown in Figs. 2(b) and 2(c). Generally, both the imaginary and real parts of the bare charge susceptibility exhibited divergence at the same wave vector $\boldsymbol{Q}$, indicating that Fermi surface nesting can contribute to the CDW phase transition. As the direction of $\boldsymbol{Q}$ was parallel to the Ta-chains in the $TaIrTe_4$ monolayer,[16] a vector aligned with the Nb-chains in the $NbIrTe_4$ monolayer was selected for further analysis. From Figs. 2(b), 2(c), and Fig. S1 in Supplementary Information, a local maximum simultaneously appeared in both the imaginary and real components at the wavevectors $\boldsymbol{Q}^{*1} = (0, 0.047\frac{2\pi}{a})$ and $\boldsymbol{Q}^{*2} = (0, 0.049\frac{2\pi}{b})$ for the valence and conduction bands, respectively. Therefore, a CDW phase transition may occur when the chemical potential is shifted near $\sim E_F + 60$ meV and $\sim E_F - 60$ meV via weak doping or gating effects.

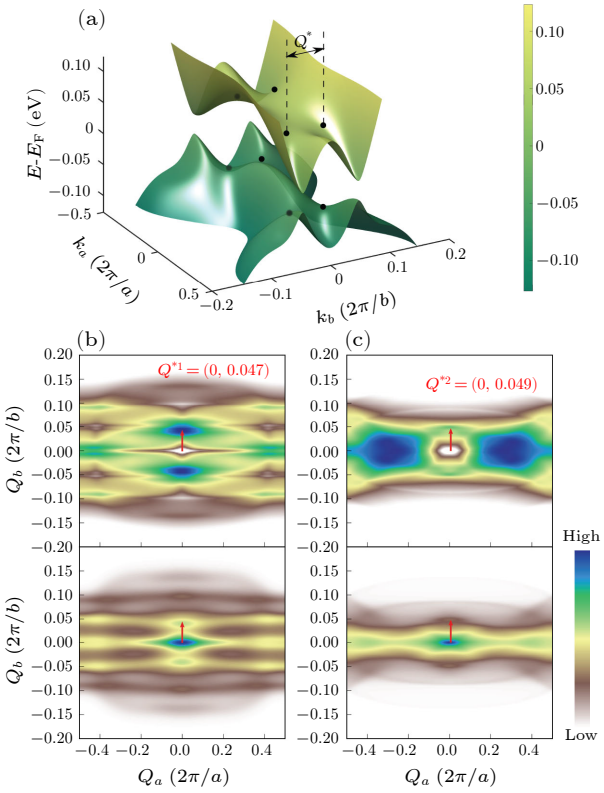

Fig. 2. Band structure and charge susceptibility in the $NbIrTe_4$ monolayer primitive cell. (a) Three-dimensional (3D) plot of the energy dispersion ($k_a - k_b - E$) and location of VHSs near the Fermi level. (b) and (c) Real part (upper panel) and imaginary part (lower panel) of the bare charge susceptibility of $NbIrTe_4$ with the chemical potential at the VHS levels of the valence and conduction bands, respectively.

The wavevectors of $\boldsymbol{Q}^{*1} = (0, 0.047\frac{2\pi}{a})$ and $\boldsymbol{Q}^{*2} = (0, 0.049\frac{2\pi}{b})$ in Fig. 2 were characterized by supercells of dimensions $1 \times 21 \times 1$ and $1 \times 20 \times 1$, respectively. To study the possible CDW phase transitions, effective Hamiltonian models were constructed for supercells of $1 \times 21 \times 1$ and $1 \times 20 \times 1$. This was based on the overlaps of the Wannier orbitals following the Fröhlich–Peierls Hamiltonian approach with a supercell along the b-axis. Only the intra-orbital interactions were considered. The periodicity of the potential induced by the superlattice was determined by the parameter Q, which was replaced by $\boldsymbol{Q}^{*1}$ and $\boldsymbol{Q}^{*2}$.

For the $1 \times 20 \times 1$ supercell, upon increasing the potential V, a new band gap emerged near $E_F + 80$ meV, originating from the original VHSs, as illustrated by the pink range in Fig. 3(a). However, when the potential V varied from 0.01 to 0.15 eV, no indirect band gap was observed between VB - 1 and VB - 10 for the VHSs below the charge neutrality point. A similar feature was observed in the $1 \times 21 \times 1$ supercell. Thus, this study focused on the $1 \times 20 \times 1$ supercell for further analysis. The absence of an indirect band gap in the valence bands may be ascribed to the competition between the detailed shape of the electronic band structure and the strength of the modulation potential. As mentioned previously, the conduction band of $NbIrTe_4$ was flatter than the valence band along the high-symmetry path Γ-X. In contrast, the conduction and valence bands of $TaIrTe_4$ exhibited almost mirror-symmetrical characteristics along this path. Figure 3(a) shows that there were two global band gaps in the energy window from $\sim E_F - 150$ to $\sim E_F + 150$ meV. One was located at the charge neutrality point and the other was generated between CB + 4 and CB + 6. The band gaps at and above the charge neutrality point were approximately 12 and 10 meV, respectively, when the modulation potential V was set to 0.1 eV. Additionally, a detailed evolution of the band gap and the topological invariant Z_2 was calculated for supercells ranging from $1 \times 14 \times 1$ to $1 \times 24 \times 1$ with a 0.1 eV modulation potential V (Figs. S2–S5).

To determine the topological charges of the two gaps, the bulk Wannier center evolutions and energy dispersions of the edge states were calculated. Figure 3(b) shows the Wannier center evolutions by modulating the chemical potential at the charge neutrality point. Each pair of evolution lines exhibited a fixed partner and degenerated at two time-reversal-invariant points, $k_x = 0$ and π/a. Therefore, the Wannier center evolutions did not intersect with the reference lines, indicating that the gap at the

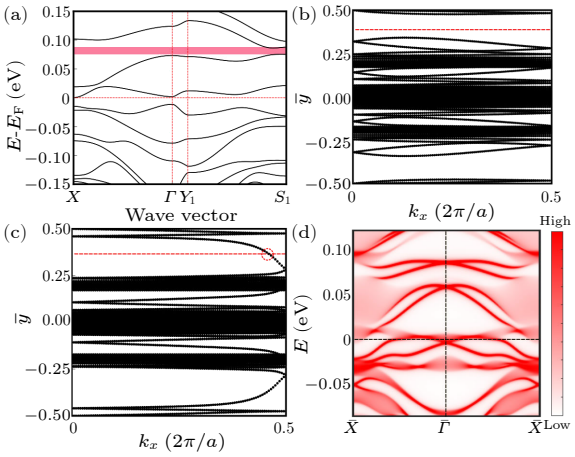

Fig. 3. Band structure and topological properties in the CDW phase. (a) Energy dispersion along the high-symmetry paths. The pink range represents the VHS generated Z_2 band gap. (b) and (c) Wannier charge center evolutions with the Fermi level lying at E_0 and $E_0 + 80$ meV, respectively. (d) Energy dispersion of the edge states.

charge neutrality point was topologically trivial. However, the Wannier center evolutions switched partners at $k_x = 0$ and π/a, while keeping the occupied bands fixed at CB +4, as shown in Fig. 3(c). The zigzag pattern of the Wannier center evolutions ensured an odd number of intersections with the reference lines, demonstrating the emergence of a non-trivial Z_2 band gap.

The topological phases were further verified by calculating the edge states with open boundary conditions along the b-axis. From the energy dispersion illustrated in Fig. 3(d), the three zones indexed by energy windows from $\sim E_F - 40$ to $\sim E_F + 10$ meV, $\sim E_F + 10$ to $\sim E_F + 60$ meV, and $\sim E_F + 60$ to $\sim E_F + 100$ meV are of most interest. In the first region, although edge bands were present within the bulk band gap, they intersected the Fermi level twice. Consequently, these edge states lacked topological protection and were eliminated through external perturbations, which is consistent with the behavior exhibited by the Wannier center evolutions depicted in Fig. 3(b). In the second region, a Dirac-point-like edge band structure connecting the bulk states originating from CB + 2 and CB + 4 was observed, as shown in Fig. 3(a). There was a noticeable band anti-crossing between CB + 2 and CB + 4 around the X point, although there was no indirect band gap. Therefore, the band structures resulting from CB + 2 and CB + 4 formed a non-trivial Z_2 topological semimetal state when considering the CDW modulation potential. This differs from the case of monolayer $TaIrTe_4$, in which a direct non-trivial Z_2 band gap of approximately 5 meV was formed by CB + 2 and CB + 4.

While there was no global band gap between CB + 2 and CB + 4, a direct gap was formed by CB + 4 and CB + 6 in the range from $\sim E_F + 60$ to $\sim E_F + 100$ meV. From the edge energy dispersion in this energy window, a Dirac-point state connecting the bulk bands originated from the original CB + 4 and CB + 6. This is a typical feature of a 2D Z_2 topological insulator and fully agrees with the analysis of the Wannier charge center evolutions in Fig. 3(c). Therefore, $NbIrTe_4$ was expected to undergo a CDW phase transition along the b-axis, resulting in two non-trivial Z_2 band gaps: a direct band gap with a globally semi-metallic nature, and an indirect band gap of approximately 10 meV. As both gaps were close to the charge neutrality point, they were achieved via weak electron doping or gating.

4. Conclusion. In summary, a dual QSHI state was predicted in monolayer $NbIrTe_4$ via first-principles calculations. In addition to the original non-trivial Z_2 band gap at the charge neutrality point, a new global Z_2 band gap of approximately 10 meV emerged when the chemical potential was shifted to the VHS point in the electron doping range. In addition, an indirect band inversion in the CDW phase was observed in the energy window at approximately $E_0 + 20$ to $E_0 + 30$ meV near the X point. Given that both these non-trivial band gaps were situated close to the charge neutrality point, they were likely to be detected experimentally through weak electron doping or gating. Moreover, the VHS point above the Fermi level was dominated by the 4d orbitals of Nb. Compared with the Ta 5d orbitals in $TaIrTe_4$, the dual QSHI state in $NbIrTe_4$ is expected to show stronger correlation effects, potentially leading to the emergence of additional correlated topological states.

Acknowledgements. This work was supported by the National Key R&D Program of China (Grant No. 2021YFB3501503), the National Natural Science Foundation of China (Grant Nos. 52271016 and 52188101), and the Foundation of Liaoning Province (Grant No. XLYC2203080). Some numerical calculations in this study were performed using the ORISE Supercomputer.

References

[1] Wang L, Shih E M, Ghiotto A, Xian L, Rhodes D A, Tan C, Claassen M, Kennes D M, Bai Y, Kim B, Watanabe K, Taniguchi T, Zhu X, Hone J, Rubio A, Pasupathy A N, and Dean C R 2020 *Nat. Mater.* **19** 861

[2] Liu G B, Xiao D, Yao Y, Xu X, and Yao W 2015 *Chem. Soc. Rev.* **44** 2643

[3] Hsu Y T, Vaezi A, Fischer M H, and Kim E A 2017 *Nat. Commun.* **8** 14985

[4] Wei L, Xu Q, He Y, Li Q, Huang Y, Zhu W, Watanabe K, Taniguchi T, Claassen M, Rhodes D A, Kennes D M, Xian L, Rubio A, and Wang L 2024 *Proc. Natl. Acad. Sci.* **121** e2321665121

[5] Kim K, Kim S, Kim J S, Kim H, Park J H, and Min B I 2018 *Phys. Rev. B* **97** 165102

[6] Xu S, Al Ezzi M M, Balakrishnan N, Garcia-Ruiz A, Tsim B, Mullan C, Barrier J, Xin N, Piot B A, Taniguchi T, Watanabe K, Carvalho A, Mishchenko A, Geim A K, Fal'ko V I, Adam S, Neto A H C, Novoselov K S, and Shi Y 2021 *Nat. Phys.* **17** 619

[7] Wu S, Zhang Z, Watanabe K, Taniguchi T, and Andrei E Y 2021 *Nat. Mater.* **20** 488

[8] Lee K, Lange G F, Wang L L, Kuthanazhi B, Trevisan T V, Jo N H, Schrunk B, Orth P P, Slager R J, Canfield P C, and Kaminski A 2021 *Nat. Commun.* **12** 1855

[9] Kang M, Ye L, Fang S, You J S, Levitan A, Han M, Facio J I, Jozwiak C, Bostwick A, Rotenberg E, Chan M K, Mc-

Donald R D, Graf D, Kaznatcheev K, Vescovo E, Bell D C, Kaxiras E, van den Brink J, Richter M, Prasad Ghimire M, Checkelsky J G, and Comin R 2020 *Nat. Mater.* **19** 163
[10] Lu J L, Luo W, Li X Y, Yang S Q, Cao J X, Gong X G, and Xiang H J 2017 *Chin. Phys. Lett.* **34** 057302
[11] Xu Y, Yan B, Zhang H J, Wang J, Xu G, Tang P, Duan W, and Zhang S C 2013 *Phys. Rev. Lett.* **111** 136804
[12] Sun B, Zhao W, Palomaki T, Fei Z, Runburg E, Malinowski P, Huang X, Cenker J, Cui Y T, Chu J H, Xu X, Ataei S S, Varsano D, Palummo M, Molinari E, Rontani M, and Cobden D H 2022 *Nat. Phys.* **18** 94
[13] Guo P J, Lu X Q, Ji W, Liu K, and Lu Z Y 2020 *Phys. Rev. B* **102** 041109
[14] Liu J, Wang H, Fang C, Fu L, and Qian X 2017 *Nano Lett.* **17** 467
[15] Marrazzo A, Gibertini M, Campi D, Mounet N, and Marzari N 2019 *Nano Lett.* **19** 8431
[16] Tang J, Ding T S, Chen H, Gao A, Qian T, Huang Z, Sun Z, Han X, Strasser A, Li J, Geiwitz M, Shehabeldin M, Belosevich V, Wang Z, Wang Y, Watanabe K, Taniguchi T, Bell D C, Wang Z, Fu L, Zhang Y, Qian X, Burch K S, Shi Y, Ni N, Chang G, Xu S Y, Ma Q 2024 *Nature* **628** 515
[17] Maciejko J, Qi X L, Karch A, and Zhang S C 2010 *Phys. Rev. Lett.* **105** 246809
[18] Santos L, Neupert T, Ryu S, Chamon C, and Mudry C 2011 *Phys. Rev. B* **84** 165138
[19] Goerbig M O 2012 *Eur. Phys. J. B* **85** 15
[20] Li W, Sheng D, Ting C, and Chen Y 2014 *Phys. Rev. B* **90** 081102
[21] Wang C and Senthil T 2016 *Phys. Rev. X* **6** 011034
[22] Barkeshli M, Bonderson P, Cheng M, and Wang Z 2019 *Phys. Rev. B* **100** 115147
[23] Park K S and Han H 2010 *Phys. Rev. B* **82** 153101
[24] Ghimire N J and Mazin I I 2020 *Nat. Mater.* **19** 137
[25] Paschen S and Si Q 2021 *Nat. Rev. Phys.* **3** 9
[26] Hasan M Z and Kane C L 2010 *Rev. Mod. Phys.* **82** 3045
[27] Teng X, Chen L, Ye F, Rosenberg E, Liu Z, Yin J X, Jiang Y X, Oh J S, Hasan M Z, Neubauer K J, Gao B, Xie Y, Hashimoto M, Lu D, Jozwiak C, Bostwick A, Rotenberg E, Birgeneau R J, Chu J H, Yi M, and Dai P 2022 *Nature* **609** 490
[28] Yin J X, Lian B, and Hasan M Z 2022 *Nature* **612** 647
[29] Yin J X, Ma W, Cochran T A, Xu X, Zhang S S, Tien H J, Shumiya N, Cheng G, Jiang K, Lian B, Song Z, Chang G, Belopolski I, Multer D, Litskevich M, Cheng Z J, Yang X P, Swidler B, Zhou H, Lin H, Neupert T, Wang Z, Yao N, Chang T R, Jia S, and Zahid Hasan M 2020 *Nature* **583** 533
[30] Yin J X, Zhang S S, Li H, Jiang K, Chang G, Zhang B, Lian B, Xiang C, Belopolski I, Zheng H, Cochran T A, Xu S Y, Bian G, Liu K, Chang T R, Lin H, Lu Z Y, Wang Z, Jia S, Wang W, and Hasan M Z 2018 *Nature* **562** 91
[31] Kang M, Fang S, Ye L, Po H C, Denlinger J, Jozwiak C, Bostwick A, Rotenberg E, Kaxiras E, Checkelsky J G, and Comin R 2020 *Nat. Commun.* **11** 4004
[32] Guo C, Wagner G, Putzke C, Chen D, Wang K, Zhang L, Gutierrez-Amigo M, Errea I, Vergniory M G, Felser C, Fischer M H, Neupert T, and Moll P J W 2024 *Nat. Phys.* **20** 579
[33] Wang Y, Liu Y, Hao Z, Cheng W, Deng J, Wang Y, Gu Y, Ma X M, Rong H, and Zhang F 2023 *Chin. Phys. Lett.* **40** 037102
[34] Aramberri H and Muñoz M C 2017 *Phys. Rev. B* **95** 205422
[35] Jeffries J, Butch N, Vohra Y, and Weir S 2015 *J. Phys.: Conf. Ser.* **592** 012124
[36] Lee C C, Xu S Y, Huang S M, Sanchez D S, Belopolski I, Chang G, Bian G, Alidoust N, Zheng H, Neupane M, Wang B, Bansil A, Hasan M Z, and Lin H 2015 *Phys. Rev. B* **92** 235104
[37] Sun Y, Wu S C, and Yan B 2015 *Phys. Rev. B* **92** 115428
[38] Chang C Z, Zhang J, Feng X, Shen J, Zhang Z, Guo M, Li K, Ou Y, Wei P, Wang L L, Ji Z Q, Feng Y, Ji S, Chen X, Jia J, Dai X, Fang Z, Zhang S C, He K, Wang Y, Lu L, Ma X C, Xue Q K 2013 *Science* **340** 167
[39] Hafner J 2008 *J. Comput. Chem.* **29** 2044
[40] Garrity K F, Bennett J W, Rabe K M, and Vanderbilt D 2014 *Comp. Mater. Sci.* **81** 446
[41] Mostofi A A, Yates J R, Lee Y S, Souza I, Vanderbilt D, and Marzari N 2008 *Comput. Phys. Commun.* **178** 685
[42] Fröhlich H. 1954 *Proc. Natl. Acad. Sci.* **223** 296
[43] Johannes M and Mazin I 2008 *Phys. Rev. B* **77** 165135
[44] Empante T A, Zhou Y, Klee V, Nguyen A E, Lu I H, Valentin M D, Naghibi Alvillar S A, Preciado E, Berges A J, Merida C S, Gomez M, Bobek S, Isarraraz M, Reed E J, Bartels L 2017 *ACS nano* **11** 900
[45] Lv M, Yu G, and Chen W 2022 *Inorg. Chem. Front.* **9** 6133
[46] Bryant G W 1985 *Phys. Rev. B* **31** 5166
[47] Soluyanov A A and Vanderbilt D 2011 *Phys. Rev. B* **83** 035108